Since January 2020 Elsevier has created a COVID-19 resource centre with free information in English and Mandarin on the novel coronavirus COVID-19. The COVID-19 resource centre is hosted on Elsevier Connect, the company's public news and information website.

Journal of Hazardous Materials 402 (2021) 123472

Contents lists available at ScienceDirect

Journal of Hazardous Materials

journal homepage: www.elsevier.com/locate/jhazmat

Pyrolysis dynamics of two medical plastic wastes: Drivers, behaviors, evolved gases, reaction mechanisms, and pathways

Ziyi Ding[a], Huashan Chen[b], Jingyong Liu[a,*], Haiming Cai[a], Fatih Evrendilek[c], Musa Buyukada[d]

[a] Guangdong Key Laboratory of Environmental Catalysis and Health Risk Control, School of Environmental Science and Engineering, Guangdong University of Technology, Guangzhou 510006, China
[b] Guoke (Foshan) Testing and Certification Co., Ltd., Foshan 528000, China
[c] Department of Environmental Engineering, Bolu Abant Izzet Baysal University, Bolu 14052, Turkey
[d] Department of Chemical Engineering, Bolu Abant Izzet Baysal University, Bolu 14052, Turkey

GRAPHICAL ABSTRACT

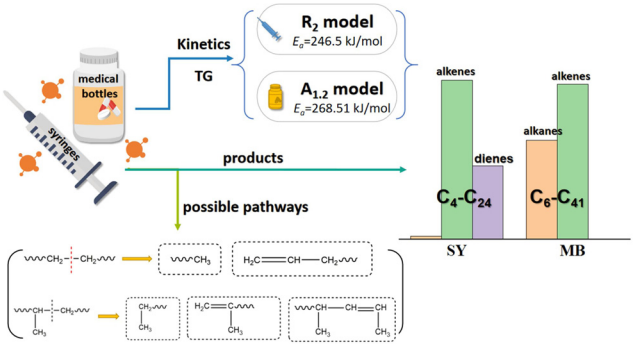

ARTICLE INFO

Editor: Daniel C.W. Tsang

Keywords:
Medical plastic wastes
Pyrolysis
Product distribution
TG-FTIR
Py-GC/MS

ABSTRACT

The public has started to increasingly scrutinize the proper disposal and treatment of rapidly growing medical wastes, in particular, given the COVID-19 pandemic, raised awareness, and the advances in the health sector. This research aimed to characterize pyrolysis drivers, behaviors, products, reaction mechanisms, and pathways via TG-FTIR and Py-GC/MS analyses as a function of the two medical plastic wastes of syringes (SY) and medical bottles (MB), conversion degree, degradation stage, and the four heating rates (5,10, 20, and 40 °C/min). SY and MB pyrolysis ranged from 394.4 to 501 and from 417.9 to 517 °C, respectively. The average activation energy was 246.5 and 268.51 kJ/mol for the SY and MB devolatilization, respectively. MB appeared to exhibit a better pyrolysis performance with a higher degradation rate and less residues. The most suitable reaction mechanisms belonged to a geometrical contraction model (R_2) for the SY pyrolysis and to a nucleation growth model ($A_{1.2}$) for the MB pyrolysis. The main evolved gases were C_4-C_{24} alkenes and dienes for SY and C_6-C_{41} alkanes and C_8-C_{41} alkenes for MB. The pyrolysis dynamics and reaction pathways of the medical plastic wastes have important implications for waste stream reduction, pollution control, and reactor optimization.

* Corresponding author.
E-mail address: Liujy@gdut.edu.cn (J. Liu).

https://doi.org/10.1016/j.jhazmat.2020.123472
Received 6 May 2020; Received in revised form 27 June 2020; Accepted 14 July 2020
Available online 15 July 2020

1. Introduction

Globally, with the technological advances and service coverage of the health sector, a large quantity of medical plastic wastes have been generated (Hong et al., 2018; Duan et al., 2008). There is an urgent need for a cleaner and safer disposal and treatment of the rapidly growing medical plastic wastes, in particular, given the raised public concern about epidemics including severe acute respiratory syndrome (SARS), coronavirus (COVID-19), and acquired immune deficiency syndrome (AIDS) (Yang et al., 2020; Wang et al., 2020). In 2018, 200 large and medium-sized cities in China generated about 817,000 tons of medical wastes (MEPC, 2019). On average, Chinese medical wastes are composed mainly of 45 % plastic, 20 % moisture, 13 % paper and cotton yarn, 10 % glass, and 12 % other materials (e.g., needle, surgical waste, and medicine) (Hong et al., 2018) and may have as high as 70 % organic content (Fang et al., 2020).

The traditional incineration of medical wastes eliminates their infectivity and pathogenicity and reduces their waste stream (Windfeld and Brooks, 2015) but generates inorganic emissions, toxic, heavy metal-containing ashes, and persistent organic pollutants (POPs) including polycyclic aromatic hydrocarbons (PAHs), polychlorinated dibenzo-p-dioxins (PCDDs), and polychlorinated dibenzofurans (PCDFs) (Zhang et al., 2020; Chen et al., 2013; Lijuan et al., 2010; Chen et al., 2009). The presence of plastic and other macromolecule organic compounds during the incineration of medical waste is the cause of PAHs release (Chen et al., 2013). Characterized by their higher heating value, high volatiles content, and low ash and water contents, the medical plastic wastes have potential to be thermochemically converted to energy (Bujak, 2015; Zhu et al., 2008). In particular, the pyrolysis technology has been demonstrated to be efficient in producing energy and value-added products as well as in reducing pollution levels compared to both incineration and the other thermochemical conversion technologies (Sharuddin et al., 2016).

The co-pyrolysis of bamboo stick, absorbent cotton, and medical respirator was found to evolve the volatiles of benzaldehyde, 2-butane, formic acid, hydrocarbons, acetic acid, H_2O, CO_2, and CO according to thermogravimetric analyzer and Fourier transform infrared spectroscopy (TG-FTIR) analysis, while their kinetics were described with the distributed activation energy model (Zhu et al., 2008; Yan et al., 2009). The pyrolysis behaviors and degradation kinetics of 14 typical medical wastes were previously determined using TG analysis (Deng et al., 2008). In the pyrolysis of mixed medical solid wastes, hydrocarbons and lipids were reported to account for about 60 % of bio-oils with a carbon chain length of C_6-C_{28} (Fang et al., 2020). The medicinal plastic bottles and infusion bags co-degraded in the inert and oxygen-containing atmospheres were found to produce toluene, styrene, benzene, and a small number of C_1-C_4 aliphatic hydrocarbons according to TG-FTIR, TG-mass spectrometric (TG-MS), and TG-gas chromatographic-mass spectrometric (TG-GC-MS) analyses (Qin et al., 2018). Despite the previous studies about the pyrolysis of medical wastes, there still exists a lack of an in-depth understanding of the reaction pathways of products, kinetic mechanisms, and thermodynamics. Also, given the diverse composition of the medical wastes, a certain knowledge gap remains to be filled about the pyrolysis of syringes versus medical bottles. Thus, this study aims to combine TG-FTIR and pyrolysis-gas chromatography-mass spectrometry (Py-GC/MS) analyses to comprehensively characterize the pyrolysis kinetics, evolved gases, and possible pathways of these two medical wastes.

From TG data, the kinetic and thermodynamic parameters and the reaction mechanism models can be derived combining the model-free and model-fitting methods (Cai et al., 2019; Qiao et al., 2019; Chen et al., 2015; Song et al., 2020). For example, the model-free methods of Kissinger-Akahira-Sunose (KAS) and Flynn-Wall-Ozawa (FWO) and the model-fitting method of the integral master-plots were combined to elucidate the three phases of the waste tea degradation mechanism using the best-fit D_3, F_2, and $F_{2.5}$ models, respectively (Cai et al., 2019). TG-FTIR and Py-GC/MS investigations should be coupled to accurately distinguish the evolved gaseous products, their functional groups, and molecular structures (Lin et al., 2017; Xu et al., 2018a; Ma et al., 2019). For example, the pyrolytic gases of waste bicycle tires were precisely quantified coupling TG-FTIR and Py-GC/MS analyses (Xu et al., 2018a). Among all the medical waste types, the medical plastic waste is characterized by its large quantity, high volatilization, high calorific value, and high organic content (Zhu et al., 2008; Yan et al., 2009), all of which enriches its utilization potential for the energy and by-product recoveries. Hence, the present study focuses on the two typical types of the medical plastic waste (syringes and medical bottles). In light of the aforementioned knowledge gaps, the objective of the present study was, for the first time, to dynamically characterize the two medical plastic wastes in terms of their pyrolysis drivers, behaviors, kinetics, thermodynamics, evolved gases, reaction mechanisms, and pathways by combining TG, TG-FTIR, Py-GC/MS, and modeling techniques.

2. Materials and methods

2.1. Preparation and characterization analyses of samples

The discarded syringes (SY) and medicine bottles (MB) samples can have pathogenic and infectious bacteria and viruses, and hence, need to be autoclaved under the high temperature for their complete inactivation. Instead, new SY and MB samples were acquired from Jiangsu Huada Medical Device Co., Ltd. and Hengshui Shenggang Medical Trading Co., Ltd, China, respectively. They were dried naturally in a good ventilation for 24 h, cut into small pieces, crushed using a pulverizer, sieved to 100 μm, and stored in a dryer. Proximate analysis was conducted according to the Chinese standard GB/T212-2008, while ultimate analysis of organic components was tested using an elemental analyzer (Vario EL cube by Elementar, Germany).

2.2. Thermogravimetric data

The thermal degradation processes were detected using a TG analyzer (NETZSCH STA 409 PC, Germany) at the four heating rates of 5, 10, 20, and 40 °C/min. About 8 mg samples were put into alumina crucibles and heated from 25 to 900 °C in the N_2 atmosphere. The flow rates of the carrier and protective gases (N_2) were 50 ml/min and 20 ml/min, respectively. To avoid the systematic errors, a bank test was conducted for each heating rate before the start of the actual experiments. The mass loss was detected as a function of temperature and time using the analyzer software.

2.3. Kinetic data

The pyrolysis kinetics were derived from the TG data thus:

$$\frac{d\alpha}{dt} = k(T)\bullet f(\alpha) \tag{1}$$

where $k(T)$ represents the reaction rate constant, while $f(\alpha)$ represents the reaction mechanism function. T, t, and α represent the absolute temperature, reaction time, and reaction conversion degree, respectively.

α and $k(T)$ can be defined as follows:

$$\alpha = \frac{m_0 - m_t}{m_0 - m_\infty} \tag{2}$$

$$k(T) = Aexp\left(-\frac{E}{RT}\right) \tag{3}$$

where m_0, m_t, and m_∞ represent the original, actual, and final masses, respectively; A, E, and R represent the pre-exponential factor (s^{-1}), the activation energy (kJ/mol), and the universal gas constant (8.314 J/mol/K). The heating rate (β) was expressed as follows:

Table 1
The common reaction mechanisms and the integral forms (Hu et al., 2019).

Symbol	Reaction mechanisms	$f(\alpha)$	$G(\alpha)$
Nucleation growth model			
A1	One-dimensional	$1.5(1-\alpha)[-\ln(1-\alpha)]^{1/3}$	$[-\ln(1-\alpha)]^{2/3}$
A2	Two-dimensional	$2(1-\alpha)[-\ln(1-\alpha)]^{1/2}$	$[-\ln(1-\alpha)]^{1/2}$
A3	Three-dimensional	$3(1-\alpha)[-\ln(1-\alpha)]^{2/3}$	$[-\ln(1-\alpha)]^{1/3}$
Diffusion			
D1	One-dimension transport	$1/(2\alpha)$	α^2
D2	Two-dimension transport	$[-\ln(1-\alpha)]^{-1}$	$(1-\alpha)\ln(1-\alpha)+\alpha$
D3	Three-dimension transport	$(3/2)(1-\alpha)^{2/3}[1-(1-\alpha)^{1/3}]^{-1}$	$[1-(1-\alpha)^{1/3}]^2$
D4	Ginstling–Brounshtein equation	$(3/2)[(1-\alpha)^{-1/3}-1]^{-1}$	$(1-2\alpha/3)-(1-\alpha)^{2/3}$
Order of reaction			
F1	First-order	$1-\alpha$	$-\ln(1-\alpha)$
F2	Second-order	$(1-\alpha)^2$	$(1-\alpha)^{-1}-1$
F3	Third-order	$(1-\alpha)^3$	$[(1-\alpha)^{-2}-1]/2$
F4	Fourth-order	$(1-\alpha)^4$	$[(1-\alpha)^{-3}-1]/3$
Geometrical contraction model			
R1	One-dimensional	1	α
R2	Two-dimensional	$2(1-\alpha)^{1/2}$	$1-(1-\alpha)^{1/2}$
R3	Three-dimensional	$3(1-\alpha)^{2/3}$	$1-(1-\alpha)^{1/3}$

$$\beta = \frac{dT}{dt} \tag{4}$$

Combining Eqs. (2) to (4) yields the following:

$$\frac{d\alpha}{f(\alpha)} = \frac{A}{\beta} exp\left(-\frac{E}{RT}\right)dT \tag{5}$$

Integrating the Eq. (5) with the initial condition of $\alpha = 0$ at $T = T_0$ yields the following:

$$G(\alpha) = \int_0^{\alpha} \frac{d\alpha}{f(\alpha)} = \frac{A}{\beta}\int_{T_0}^{T} exp\left(-\frac{E}{RT}\right)dT \approx \frac{A}{\beta}\int_0^{T} exp\left(-\frac{E}{RT}\right)dT \tag{6}$$

2.3.1. Iso-conversional methods

The three iso-conversional methods of FWO, KAS, and Starink were operated to estimate the apparent activation energy (E_a). The FWO method was defined as follows according to the Doyle's approximation:

$$\ln\beta = ln\left(\frac{AE}{RG(\alpha)}\right) - 5.331 - 1.052\left(\frac{E}{RT}\right) \tag{7}$$

Based on the Coats-Redfern approximation, the KAS method was expressed thus:

$$\ln\left(\frac{\beta}{T^2}\right) = ln\left(\frac{AR}{EG(\alpha)}\right) - \frac{E}{RT} \tag{8}$$

The Starink method was expressed thus:

$$\ln\left(\frac{\beta}{T^{1.92}}\right) = \ln\left(\frac{AR}{R(G)}\right) - 0.312 - 1.0008\frac{E}{RT} \tag{9}$$

The four thermodynamic parameters of ΔH, ΔG, ΔS, and A can be estimated from Eq. (10) to Eq. (13):

$$A = \left[\beta \bullet Ea \bullet \exp\left(\frac{E_a}{RT_p}\right)\right]/(RT_p^2) \tag{10}$$

$$\Delta H = E_a - RT \tag{11}$$

$$\Delta G = E_a + R \bullet T_P \bullet ln(\frac{K_B \bullet T_P}{h \bullet A}) \tag{12}$$

$$\Delta S = (\Delta G - \Delta H)/T_P \tag{13}$$

where K_B and h were the Boltzmann constant (1.381×10^{-23} J/K) and the Plank constant (6.626×10^{-34} J·s.), respectively.

2.3.2. Integral master-plots method

Using the FWO, KAS, and Starink-based E_a estimates and the master-plots method, the best-fit reaction mechanisms can be determined. Eq. (6) can be transformed thus:

$$G(\alpha) = \frac{AE}{\beta R}P(u) \tag{14}$$

$u = E/RT$ and $P(u)$ are the integral of temperature. $P(u)$ has no accurate solution. Applying the Doyle's approximation, $P(u)$ can be given thus (Zhang et al., 2019):

$$P(u) = 0.00484exp(-1.0516u) \tag{15}$$

For a single-step pyrolysis reaction with stationary g(α), a suitable kinetic reaction model can be confirmed using the integral master-plots with the values of A, E_a, and T estimated from the iso-conversional methods. Using the reference point of $\alpha = 0.5$, Eq. (14) can be arranged thus:

$$G(0.5) = \frac{AE}{\beta R}P(u_{0.5}) \tag{16}$$

where $u_{0.5} = E/RT_{0.5}$. The master-plots method can be shown combining Eq. (14) with Eq. (16).

$$\frac{G(\alpha)}{G(0.5)} = \frac{P(u)}{P(u_{0.5})} \tag{17}$$

$G(\alpha)/G(0.5)$ was determined factoring α into the different integral forms of the kinetic models listed in Table 1 (Hu et al., 2019). $G(\alpha)/G(0.5)$ versus α represents the theoretical master-plots. $P(u)/P(u_{0.5})$ versus α represents the experimental master-plots. Finally, the best-fit kinetic model was determined matching the theoretical and experimental master-plots. In order to verify the credibility of the selected model, MATLAB was used to reversely compute the reaction transition process predicted by the model.

2.4. TG-FTIR data

The TG-FTIR experiments were conducted using a TG analyzer (NETZSCH TG209F1) coupled with an FTIR spectrometer (NICOLET iS50 FTIR). The samples were about 8 mg. The analyzer was heated from 30 to 900 °C at 20 °C/min under the pure N_2 atmosphere. In order to avoid the condensation of gases, the transfer tubes connecting TG analyzer and FTIR spectrometer were kept at 280 °C. The FTIR spectra were analyzed at a 4-cm^{-1} resolution with 8 scans in the range of $4000-550$ cm^{-1}. To eliminate the influence of background value, blank experiments were carried out before the start of the actual experiments.

2.5. Py-GC/MS data

Py-GC/MS experiments were carried out using a pyrolysis reactor (Frontier Lab PY-2020id, Japan) coupled with a GC/MS equipped with an HP-5MS capillary column (60 m × 0.32 mm × 0.25 μm) to detect the volatiles. The sample was degraded at 650 °C for 24 s using the purified He as the carrier gas at a flow rate of 1.2 ml/min. The initial temperature of the GC/MS oven was maintained at 45 °C for 2 min, heated to 300 °C at a rate of 4 °C/min, and held on until the end of the experiments. The mass spectrum was obtained in EI mode at 70 eV. The range of the full scan mode was m/z 50 − 650. The components of volatiles were determined characterizing the GC-MS spectra according to the related literature and NIST database.

3. Results and discussion

3.1. Physicochemical drivers of pyrolysis

The moisture contents of SY and MB were close to zero, while their ash contents were 17.56 and 1.65 %, respectively. In other words, their pyrolysis generated only a small amount of ash residues, thus achieving a good volume reduction (Table 2). The volatiles content was significantly lower for SY (75.43 %) than MB (98.27 %), but their volatiles were higher than those of bamboo residues (64.55 ~ 72.95 %) (Hu et al., 2019), coal (32.37 %) (Chen et al., 2019), spent potlining (1.56 %), textile dyeing sludge (27.83 %) (Sun et al., 2019). The higher the volatiles matter is, the greater the gas production and the calorific value are, the more favorable the pyrolysis reaction is. The fixed carbon content was higher for SY (6.90 %) than MB (0.03 %). SY and MB were mainly composed of C and H. The difference in the C and H contents of SY and MB resulted in their different calorific values. Their S and N contents close to zero indicated that their thermal treatment would not produce nitrides and sulfides. The higher heating value of SY and MB (33.06 and 45.51 MJ/kg, respectively) were higher than that of coal (28.87 MJ/kg) (Chen et al., 2019), bamboo residues (17.67–18.23 MJ/kg) (Hu et al., 2019), spent potlining (22.21 MJ/kg), textile dyeing sludge (6.95 MJ/kg) (Sun et al., 2019), and coffee grounds (23.64 MJ/kg) (Chen et al., 2020). Their calorific values were higher than those of the other plastics such as polyvinyl chloride (19.02 MJ/kg) (Lee et al., 2018), polystyrene (42.3 MJ/kg) (Muneer et al., 2019), and polyethylene terephthalate (23.97 MJ/kg) (Singh et al., 2019). These results show that SY and MB have great prospects for application in the energy and by-product recoveries.

3.2. TG data-driven pyrolysis dynamics

3.2.1. Pyrolysis behaviors at 20 °C/min as a function of feedstock type, temperature, and degradation stage

The TG and derivative TG (DTG) curves of the SY and MB pyrolysis at 20 °C/min in Fig. 1 pointed to only two obvious peaks (Fig. 1a), namely, the two-stage pyrolysis process for SY. The first stage of the thermal degradation was the cracking reaction of polypropylene between 394.4 and 501 °C with a mass loss of 73.90 % and a maximum mass loss rate of 40.53 %/min at 467.3 °C (Table 3). The main component of SY was polypropylene (PP) whose pyrolysis was the free-radical irregular degradation reaction, during which chain scission occurred randomly on the main chain, generating products with a relatively low molecular weight (Singh and Sharma, 2008). Consistent with our findings, the PP pyrolysis was reported to occur between 391 and 551 °C (Xu et al., 2018b). The second stage involved the secondary cracking of the pyrolysis products, or the degradation of the recalcitrant and stable substances between 661.9 and 759.5 °C with a mass loss of 10.74 % and a maximum mass loss rate of 2.99 %/min at 738.3 °C (Table 3).

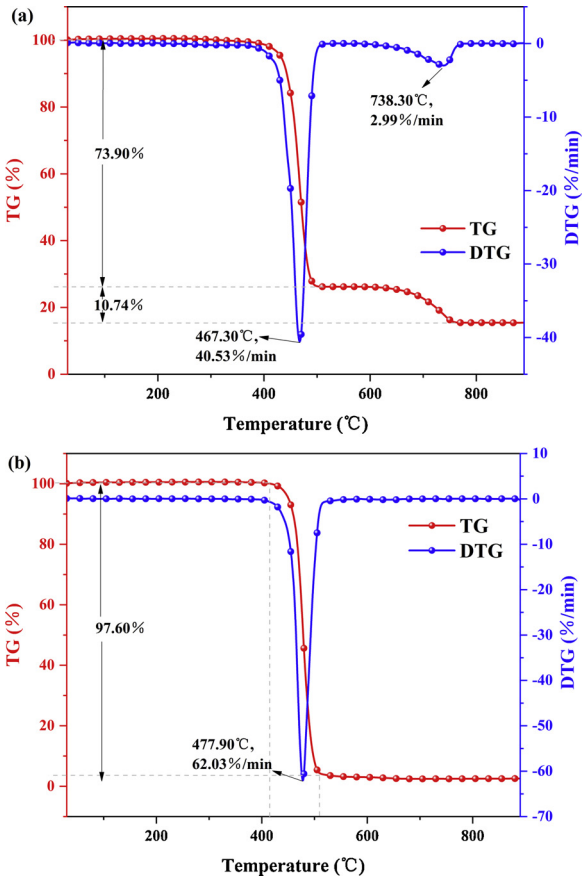

Fig. 1. (D)TG curves of (a) SY and (b) MB pyrolysis at a heating rate of 20 °C/min.

A single-stage thermal degradation process for MB occurred between 417.9 and 517 °C (Fig. 1b). A large mass loss of 97.60 % and a maximum mass loss rate of 62.03 %/min at 477.9 °C (Table 3) in this stage indicated the intense thermal degradation reaction. Our results were in close agreement with the temperature range of the polyethylene (PE) pyrolysis of 440 − 572 °C reported by (Xu et al., 2018b). As with PP, the pyrolysis of PE was a free-radical chain mechanism (Singh and Sharma, 2008), where irregular chain scission occurred generating a large number of free radicals as well as gradually synthesizing stable small molecule volatiles (Wu et al., 2014).

Table 2
The proximate analyses, ultimate analyses, and higher heating value analyses of syringes (SY) and medicine bottles (MB).

Sample	Proximate analysis (wt.%)				Ultimate analysis (wt.%)				HHV (MJ/kg)
	M	V	A	FC	C	H	N	S	
SY	0.11	75.43	17.56	6.90	66.35	10.48	0.00	0.09	33.06
MB	0.05	98.27	1.65	0.03	84.71	13.81	0.00	0.07	45.51

M = moisture; V = volatiles; A = ash; FC = fixed carbon; and HHV = higher heating value.

Table 3
Pyrolysis characteristic parameters for SY and MB at 20 °C/min.

Sample		T_o (°C)	T_p (°C)	R_p (%/min)	T_f (°C)	Weight loss (%)	Residue (%)
SY	Stage I	394.4	467.3	40.53	501.0	73.90	15.37
	Stage II	661.9	738.3	2.99	759.5	10.74	
MB	Stage I	417.9	477.9	62.03	517.0	97.60	2.40

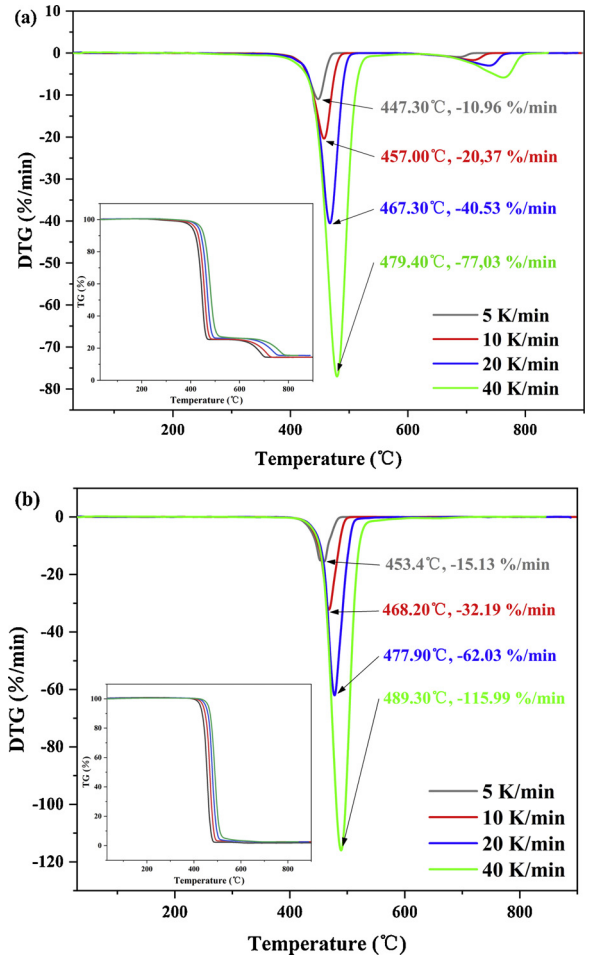

Fig. 2. (D)TG curves of (a) SY and (b) MB pyrolysis at the four heating rates.

3.2.2. Pyrolysis behaviors as a function of heating rate

The increased heating rate shifted the (D)TG curves backward (Fig. 2) due to the thermal hysteresis and the heat transfer limitation. The maximum mass loss rate of each stage grew faster with the increased heating rate. The narrowed temperature ranges of MB and SY in the first stage showed that the higher heating rate accelerated the reaction rate and reduced the reaction time. The reaction temperatures of MB and SY in the first stage at each heating rate varied between 394.4 and 517 °C during which the volatiles was most released. The DTG curve had almost the same trend which may be because PE and PP had similar chemical bonds in their molecular structures (Aboulkas et al., 2010). There existed more methyl side chains on the PP molecular chain with its higher degree of branching but its lower thermal stability than PE. Thus, the pyrolysis characteristic temperature was lower for SY than MB (Table 3). The similar residue and ash contents of both feedstocks indicated the reliability of the TG data. The devolatilization stages of the SY and MB pyrolysis occurred in the similar temperature range of 400 − 600 °C. However, MB appeared to have a better pyrolysis performance with a higher maximum weight loss rate and mass loss and less residues.

3.3. Pyrolysis kinetics as a function of feedstock type, conversion degree, and degradation stage

3.3.1. Apparent activation energy estimates according to FWO, KAS, and Starink

The higher E_a value indicated the more energy requirement to initiate the reactions due to the greater force among the sample molecules (Zou et al., 2019). The FWO, KAS, and Starink-based E_a estimates of the SY and MB pyrolysis and their best-fit lines as a function of conversion degree and degradation stage are showed in the supplementary online material (Fig. S1 and Table S1). All the coefficients of determination values (R^2) for the E_a values were in the range of 98.62–99.99 %. And a strong linear relationship was found indicating that the estimated results were reasonable. The E_a estimates did not significantly differ from one another among the methods (Table 4). The FWO-based E_a estimates of MB and SY (stages I and II) were 268.51, 246.50, and 216.98 kJ/mol, respectively. Their E_a values were higher than those of *Lentinula edodes* pileus (181.12 kJ/mol), rice husk (185.70 kJ/mol), and paper sludge (133.98 kJ/mol). In other words, they needed to break higher energy barriers (Zou et al., 2019; Minh Loy et al., 2018; Fang et al., 2015) since the higher the reaction temperature and the E_a value are, the more difficult the substance is to degrade (Chen et al., 2015). Also, the higher E_a value of MB than SY (stages I and II) showed that MB was more difficult to decompose than SY. Although MB and SY contained a large number of the C—H and C—C bonds, SY had more $-CH_3$ branches and poorer thermal stability than did MB. Thus, the less E_a requirement for the SY than MB cleavage was reflected by the fact that the initial and final pyrolysis temperatures and the maximum mass loss peak temperature were slightly lower for SY than MB.

Among the FWO, KAS, and Starink methods, the E_a value ranged from 253.36 to 277.54 kJ/mol for the MB pyrolysis, from 231.27 to 254.76 kJ/mol for the first stage, and from 200.78 to 245.14 kJ/mol for the second stage of the SY pyrolysis (Fig. 3). The E_a curve was of M-shape for the first stage of SY and of a semi-ellipsoidal shape for MB. All the E_a curves exhibited a rapid, violent process that underwent a consecutively rising-steady-falling change. Their irregular variations pointed to the degradation of PP and PE as a complex reaction process including the interactions between the chemical chain breakage and the molecular recombination (Singh et al., 2019). These complex reactions were concentrated in a narrow temperature range. Although the E_a value of MB was higher than that of SY, not only did both MB and SY have similar pyrolysis temperature ranges but also had concentrated and fast reactions, thus pointing to their high pyrolysis potential. In the second stage of SY, the E_a showed a downward trend with the increased conversion degree. This may be attributed to the degradation of the recalcitrant residues, or fixed carbon.

Table 4
The mean E_a (kJ/mol) values of the SY (stages I and II) and MB pyrolysis according to the FWO, KAS, and Starink methods.

Sample	FWO		KAS		Starink	
	E_a	R^2	E_a	R^2	E_a	R^2
MB	268.51	0.9969	270.10	0.9966	270.38	0.9966
SY stage I	246.50	0.9983	247.16	0.9981	247.44	0.9981
SY stage II	216.98	0.9971	212.03	0.9967	212.51	0.9967

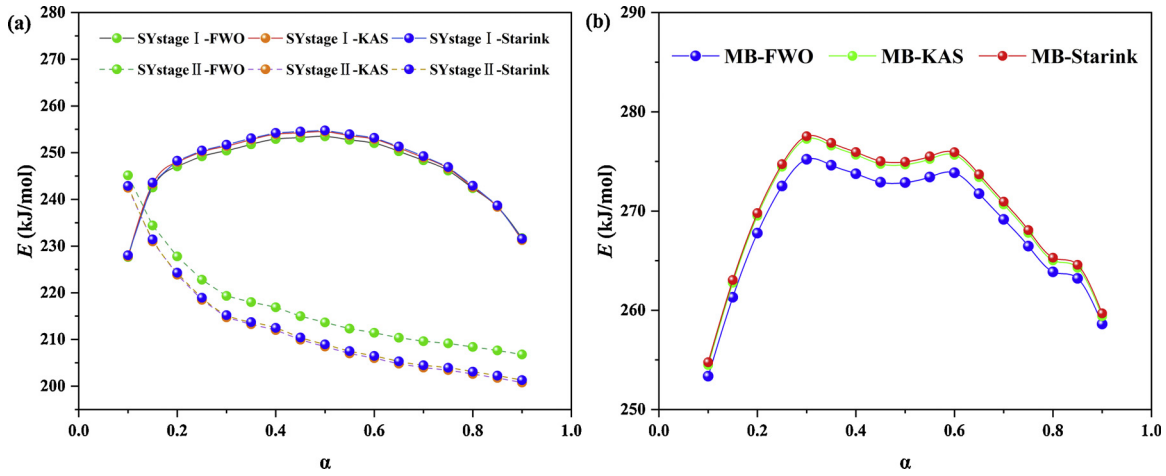

Fig. 3. Changes in E_a value of (a) SY and (b) MB pyrolysis as a function of conversion degree (α) according to the FWO, KAS, and Starink methods.

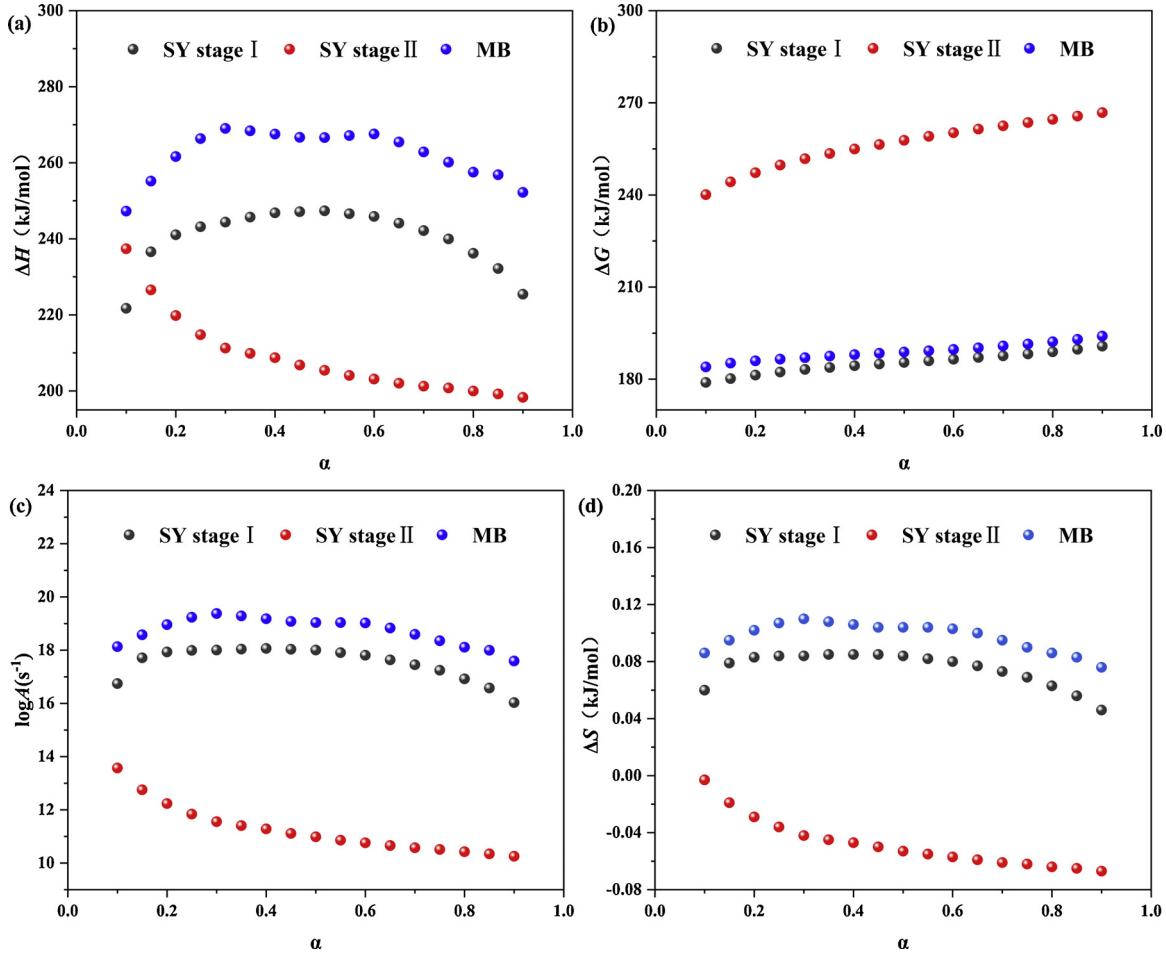

Fig. 4. The four thermodynamic parameters of the SY and MB pyrolysis at 20 ˚C/min as a function of conversion degree (α).

3.3.2. Thermodynamic parameters as a function of feedstock type, conversion degree, and degradation stage

The thermodynamic parameters (ΔG, ΔS, ΔH, and A) were estimated using the FWO method at 20 ˚C/min (Fig. 4). The higher ΔH value reflects a faster reaction rate and higher reactivity in the heat exchange between reactants and products. The similar trends of ΔH and E_a (Fig. 4a) suggested the feasibility of the reaction. The higher ΔH value of MB than SY indicated that MB needed higher energy to meet the response requirements. The smaller ΔH values than the E_a values indicated the production of more favorable pyrolysis products (Ahmad et al., 2018). The higher ΔG value represents the lower reaction feasibility given the total system energy as more energy is required to maintain the reaction. The ΔG values of SY and MB gradually rose with the increased conversion degree (Fig. 4b). The higher ΔG value in the second stage of SY related to the recalcitrant refractory substance, or the degradation of fixed carbon during which the reaction system needed to absorb more energy.

A as a measure of the collision frequency of the reactants is

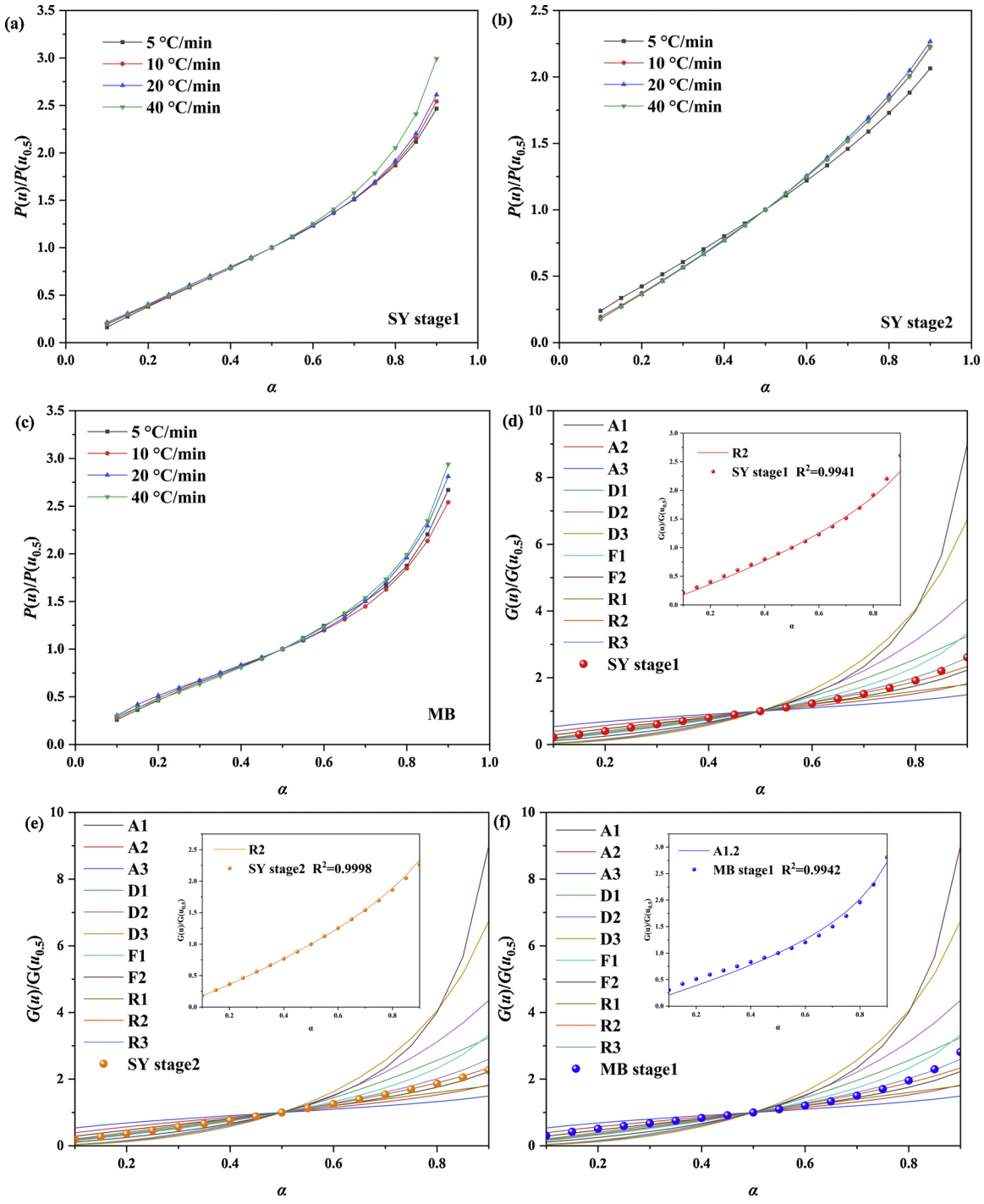

Fig. 5. Comparisons of the $P(u)/P(u_{0.5})$ versus conversion degree (α) plots for the SY pyrolysis stages (a) I and (b) II, and (c) the MB pyrolysis at the four heating rates and (d-f) at 20 °C/min to the $G(\alpha)/G(0.5)$ versus α plots for various reaction mechanisms.

determined by the intrinsic properties of the chemical reaction regardless of the reaction temperature, and the concentration of the substance in the system. The value of $A \geq 10^9\ s^{-1}$ represents a simple complex reaction, and otherwise, a complex closed reaction, or an interface reaction (Maia and de Morais, 2016). In this study, all the A values were greater than $10^9\ s^{-1}$ indicating that the SY and MB pyrolysis involved a simple complex reaction (Fig. 4c). The higher A value of MB than SY suggested a more complex MB than SY pyrolysis. Its pyrolysis complexity was mainly reflected in its diverse products, as was verified by the results of Py-GC/MS analysis in Section 3.5. ΔS reflects the disorder degree of a reaction system. The similar trends of the ΔS and log$A$ curves, with MB having a higher ΔS value than did SY also confirmed that the MB pyrolysis was more complicated than SY and produced a wide array of products.

3.3.3. Reaction mechanisms as a function of feedstock type, conversion degree, heating rate, and degradation stage

As was discussed in Section 3.3.1, since the FWO, KAS, and Starink methods estimated the similar E_a values, the integral master-plots method was performed using their average values in order to choose the most appropriate reaction mechanism for the decompositions of MB and SY. According to Eq. (15), the value of $P(u)$ can be calculated as a

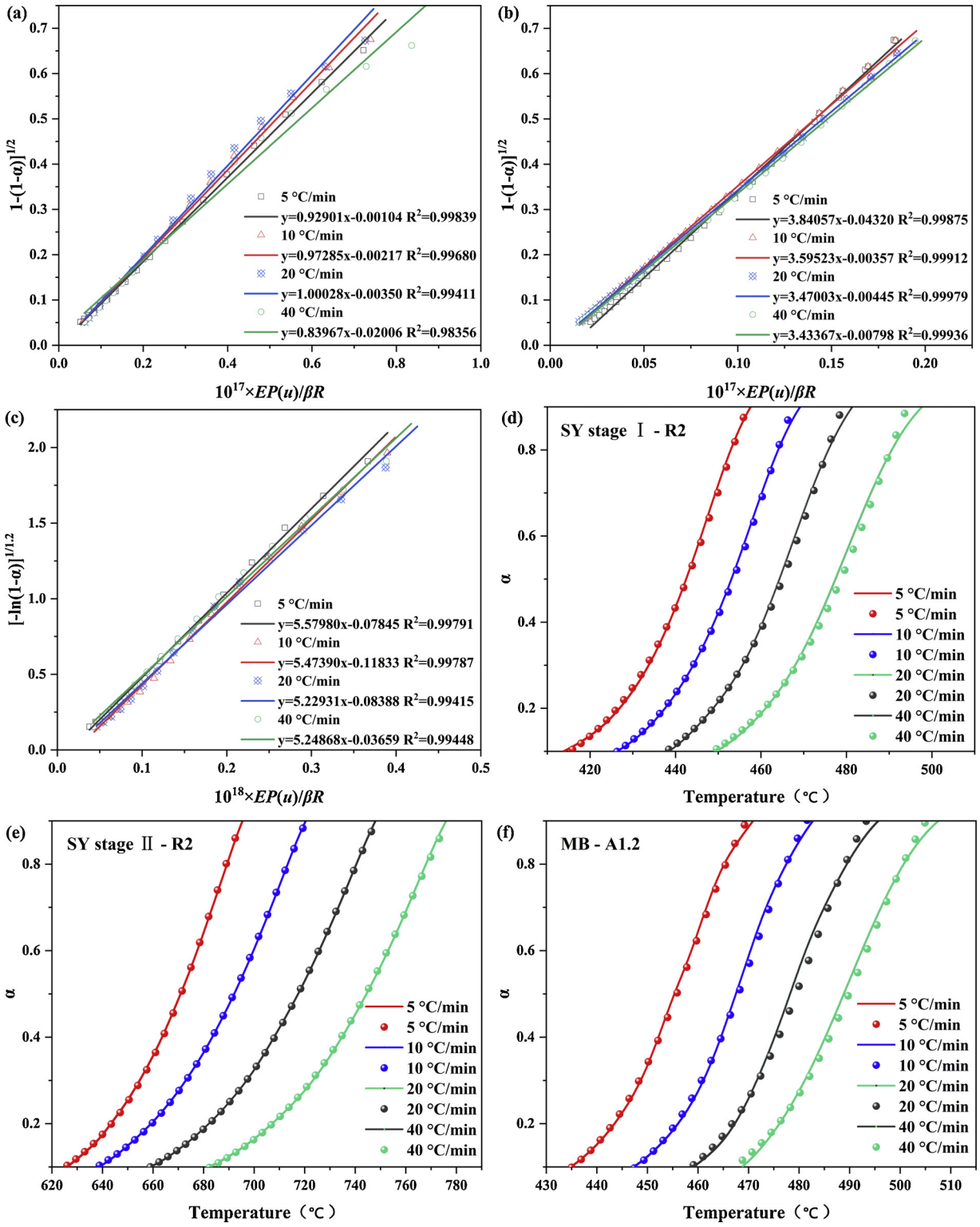

Fig. 6. The plots of $G(\alpha)$ versus $10^n \times EP(u)/\beta R$ for the SY pyrolysis stages (a) I and (b) II, and (c) the MB pyrolysis at the four heating rates; and the experimental (solid line) and predicted (dot) conversion data for the SY pyrolysis stages (d) I and (e) II, and (f) the MB pyrolysis at the four heating rates.

function of conversion degree ($\alpha = 0.1-0.9$) and the average E_α values. The plots of $P(u)/P(u_{0.5})$ versus conversion degree (α) at the four heating rates (Fig. 5a–c) emphasized that the reaction mechanisms of each stage of the SY and MB pyrolysis can be described as a single model regardless of the heating rate (Irmak Aslan et al., 2017). Since the plots of $P(u)/P(u_{0.5})$ under the four heating rates were basically identical, 20 °C/min was selected to preliminarily determine the kinetic mechanisms, and the predicted values were verified using the reverse calculations. The theoretical master-plots of $G(\alpha)/G(0.5)$ (Table 1) were compared to the experimental master-plots $P(u)/P(u_{0.5})$ at 20 °C/min in order to determine the appropriate reaction mechanisms (Fig. 5d–f). The comparisons of the plots at 20 °C/min showed that the R_2, in-between R_2 and R_3, and A_n models best described the first and second stages of the SY pyrolysis and the entire MB pyrolysis in the following

Table 5
Kinetic triplets of E_a, A, and f(a) for the SY (stages I and II) and MB pyrolysis at the four heating rates according to the master-plots method.

Sample	β (°C/min)	E_a (kJ/mol)	f (α)	A (s^{-1})	R^2
SY stage I	5	247.03	$2(1-\alpha)^{1/2}$	0.9290×10^{17}	0.9984
	10			0.9728×10^{17}	0.9968
	20			1.0002×10^{17}	0.9941
	40			0.8396×10^{17}	0.9836
SY stage II	5	213.84	$2(1-\alpha)^{1/2}$	3.8405×10^{17}	0.9988
	10			3.5952×10^{17}	0.9991
	20			3.4700×10^{17}	0.9998
	40			3.4336×10^{17}	0.9994
MB	5	269.66	$1.2(1-\alpha)[-\ln(1-\alpha)]^{1/1.2}$	5.5798×10^{18}	0.9979
	10			5.4739×10^{18}	0.9979
	20			5.2293×10^{18}	0.9942
	40			5.2486×10^{18}	0.9945

two general forms of R_n and A_n: $G(\alpha) = 1\text{-}(1\text{-}\alpha)^{1/2}$ and $G(\alpha) = [-\ln(1\text{-}\alpha)]^n$, respectively.

3.3.4. Pre-exponential factor and order estimates of the reaction mechanisms

The optimal order (n) of the reaction mechanism models was found factoring the integral function of the R_n and A_n models into Eq. (14) thus:

$$G(\alpha) = \frac{AE}{\beta R} P(u) = 1 - (1 - \alpha)^{1/n} \quad (18)$$

$$G(\alpha) = \frac{AE}{\beta R} P(u) = [-\ln(1 - \alpha)]^{1/n} \quad (19)$$

In order to determine the optimal value of n, the plots of $1\text{-}(1\text{-}\alpha)^{1/n}$ versus $EP(u) / \beta R$ and $[-\ln(1\text{-}\alpha)]^{1/n}$ versus $EP(u) / \beta R$ were made factoring the various n values (at an interval of 0.1). The best-fit regression lines with the highest R^2 values when their intercepts were closest to zero were used to select the optimal n value. The optimal values of n for the SY pyrolysis stages I and II, and the MB pyrolysis are shown in Fig. 6a–c. The kinetic triplets of E_a, A, and f(α) for the SY pyrolysis stages I and II, and the MB pyrolysis at the four heating rates were given in Table 5. As a result, R_2, and $A_{1.2}$ were determined as the most suitable models of the reaction mechanisms to explain the SY pyrolysis stages I and II and the MB pyrolysis, respectively. To verify the reliability of kinetic results, the experimental and predicted values of the SY and MB conversion degrees as a function of temperature at the four heating rates (Fig. 6d–f) were compared and found to be almost identical, thus pointing to the accuracy of their best-fit reaction mechanisms of R_2 and $A_{1.2}$ for the SY and MB pyrolysis, respectively.

3.4. TG-FTIR-detected pyrolytic functional groups and gases

Fig. 7a–c shows the FTIR spectrum at the DTG peak temperature for the SY and MB pyrolysis at 20 °C·min^{-1}. According to the Lambert-Beer law (the positive correlation between the gaseous product concentration and the absorption peak intensity), the absorbance values of the main gases as a function of temperature are showed in Fig. 7d–e. The main functional groups and vibrational modes are provided in the supplementary online material (Table S2).

According to the FTIR spectrum of the SY pyrolysis stage I (Fig. 7a), the strong absorption peaks in the range of 2960–2850 cm^{-1} proved the existence of methylene (–CH_2–) group. The characteristic absorption peaks in the ranges of 3080–3000 and 1700–1610 cm^{-1} were associated with the =C–H and C=C stretching vibrations, respectively, indicative of the formation of alkenes. The appearance of the R-CH=CH_2 bending vibration in the range of 1040–1370 cm^{-1} showed the existence of alkenes. The absorption peak in the range of 1455–1370 cm^{-1} was associated with the -CH_3 bending vibration, indicative of the formation of alkanes, in particular, CH_4 (Kai et al., 2017). The weak peaks in the range of 1325–1000 cm^{-1} can be ascribed to the stretching vibrations of C–O and O–H, indicative of the formations of phenols, alcohols, and ethers. The irregular chain break occurred with the pyrolysis of PP. Alkanes and alkenes were the main gas products of the PP pyrolysis (Qin et al., 2018). As for the SY pyrolysis stage II, CO_2 was the main volatiles product, and a small amount of –CH_2– group was observed (Fig. 7b). The obvious absorption peaks in the range of 2402–2240 cm^{-1} and in 669 cm^{-1} can be attributed to the C=O stretching vibration and the C=O bending vibration, respectively, as was evidenced by the formation of CO_2. The release of CO_2 may be due to the pyrolysis of the more stable O-containing functional groups (Zhang et al., 2019).

The FTIR spectra of the MB pyrolysis and the SY pyrolysis stage I were similar including the =C–H, $-CH_2$, C=C, $-CH_3$, and R–CH=CH_2 groups. A weak peak in the range of 716−724 cm^{-1} related to the wagging vibration of $-CH_2$. As with the PP pyrolysis, the irregular chain scission occurred during the PE pyrolysis with its main products as alkanes and alkenes. The concentration curves of the main volatiles as a function of temperature are illustrated in Fig. 7d-e. The absorbance trends of the various functional groups were consistent with the DTG curves. The SY pyrolysis stag I and the MB pyrolysis had a rapid degradation producing a large amount of alkanes and alkenes in a short period of time. The highest content of methylene together with the fewer C=C bonds indicated that the products contained many long-chain hydrocarbons. However, the results of TG-FTIR analysis needs to be supplemented by PY-GC/MS analysis, as was performed in the next section.

3.5. Py-GC/MS-detected molecular structures of pyrolytic gases

The experiments of the SY and MB pyrolysis were carried out at 650 °C, and the detailed data of the main evolved gases are presented in the supplementary online material (Table S3). The compound types of the pyrolytic products were significantly more diverse for MB than SY. By comparing their peak areas (PA), the gas distributions of the SY and MB pyrolysis are illustrated in Fig. 8. The main products of the SY pyrolysis were C_4-C_{24} alkenes (PA = 51.28 %) among which the highest content belonged to 1-heptene, 2,4-methyl- (PA = 17.66 %). 23.63 % diene and a few alkanes (PA = 1.04 %) such as pentacosane, hexacosane, and heptadecay were also detected. Similarly, alkenes as the main compounds together with the low concentrations of alkanes and dienes were previously reported as the main PP pyrolysis products (Moya et al., 2011). 2-alkenes were similarly detected as the PP pyrolysis products by (Luda and Dall'Anese, 2014). The main products of the MB pyrolysis were C_6-C_{41} alkanes (PA = 31.91 %) and C_8-C_{41} alkenes (PA = 49.94 %). The results of Py-GC/MS analysis verified that the main pyrolysis products were the longer-chain aliphatic hydrocarbons.

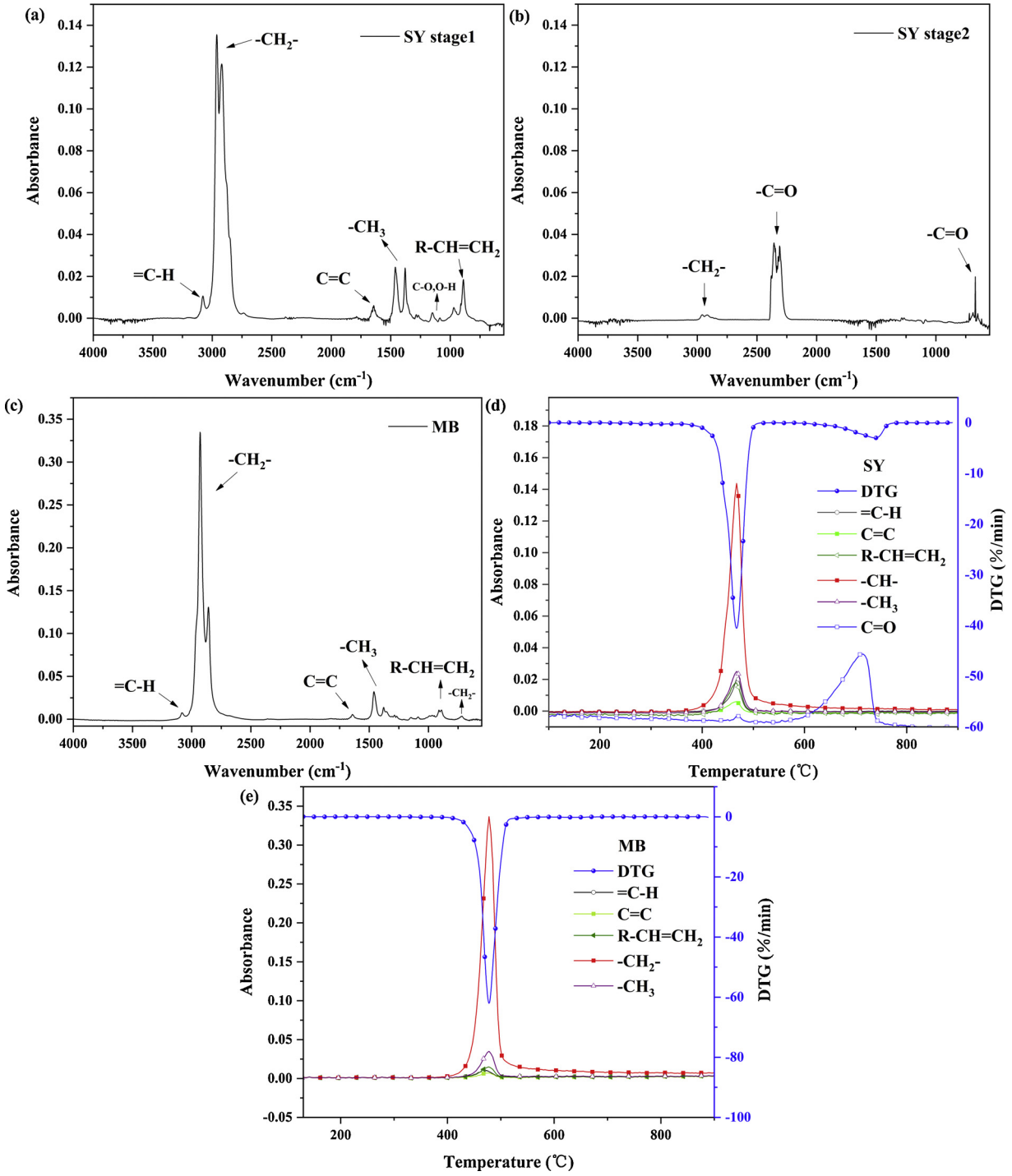

Fig. 7. The FTIR spectrum of the MB and SY pyrolysis products: (a) SY at 467.3 °C, (b) SY at 738.3 °C, and (c) MB at 477.9 °C, and the temperature-dependent absorbance for (d) SY and (e) MB.

3.6. Possible pyrolysis pathways

The possible cracking pathways of the SY and MB pyrolysis were analyzed according to the volatiles identified from the Py-GC/MS experiments (Figs. 9 and 10). Mechanistically, the polymer pyrolysis involves a complex series of free-radical reactions, synergistic reactions, or ionic reactions that occur through a number of competing pathways (Zhou et al., 2016). The PP pyrolysis products as the main SY component can be explained by the mechanism of the intramolecular H transfer after random cleavage (Luda and Dall'Anese, 2014). The intramolecular transfer of the secondary radicals plays an important role in the degradation of PP (Ma et al., 2015). The PP pyrolysis is a random chain-breaking process that produces free radicals with a different degree of polymerization (Straka et al., 2017).

The variety of low molecular weight hydrocarbons detected was the consequence of the multiple intermolecular H transfers through which the initially formed free radicals were evolved before the β-scission occurred. Due to its molecular structure, the random and variable intermolecular H transfer may occur on the secondary or tertiary C atoms of the chain. The intermolecular H transfer usually occurs in the form of 1→3, 1→4, 1→5, 1→6 to the tertiary C atoms, while the β-scission leads to the formation of 1-alkenes. (Fig. 9; steps 2 and 3). The

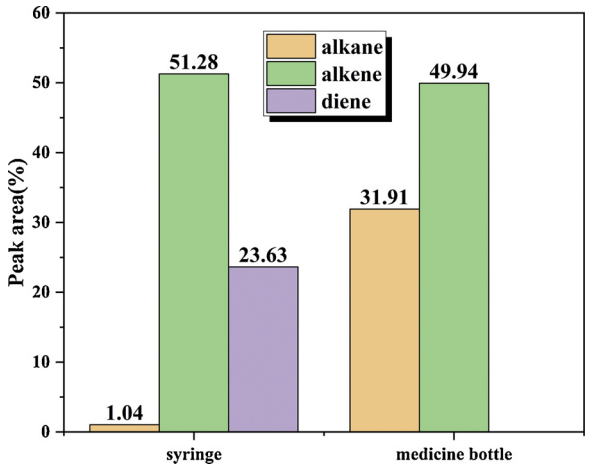

Fig. 8. The gas distributions of the SY and MB pyrolysis.

evolution of the intermolecular H transfer and β-scission during the SY pyrolysis was simulated. Thus, the two terminal structures ($-CH_2CH_2CH_3$ or $-CH_2CH(CH_3)-CH_3$) and the four possible structures of products were identified (Fig. 9). The formation of saturated alkanes was due to the β-scission and the intermolecular H abstraction reaction (Qin et al., 2018) (Fig. 9; steps 4 and 8). When the intermolecular H transfer appeared on a secondary C on the chain, 2-alkenes were formed, as was presented in Fig. 9 and step 6. 1-alkenes, 2-alkenes, and alkanes identified via Py-GC/MS analysis demonstrated that the cracking process was involved in the SY pyrolysis.

As with the SY pyrolysis, the MB pyrolysis was a random chain scission reaction (Sharuddin et al., 2016). The mechanisms of the intermolecular H transfer, the β-scission, and the intermolecular H abstraction were also involved in the MB pyrolysis. MB was mainly composed of PE. Since PE had no branch chains, its reaction process was simpler than the PP reaction. Free radicals underwent the β-scission, the intermolecular H transfer, and the intermolecular H abstraction and formed the long-chain alkanes and alkenes with different C numbers (Fig. 10).

MB was cracked randomly and generated the long-chain free radicals in different lengths. Alkenes and alkyl radicals were generated by the intermolecular H transfer and the β-scission (Fig. 10; step 3). A part of the alkyl radicals involved an intermolecular abstraction to form chain alkanes (Fig. 10; step 4). The compounds that lost H underwent the β-scission to generate the smaller molecular weight alkenes (Fig. 10; step 5). The other part of the alkyl radical could be cycled through steps 2 and 3. Fig. 11 shows the additional pyrolysis mechanisms of 1-butene, 2-pentene, 2-methyl-1-pentene and 1,8-nonadiene, 2,4,6,8-tetramethyl-(C13 diene). The disproportionation can lead to the formation of dienes (Luda and Dall'Anese, 2014), while the long-chain alkenes may undergo a series of reactions (random cracking, intermolecular H transfer, and β-scission) again (Fig. 11D).

Overall, alkanes and alkenes were the main products of the SY and MB pyrolysis. Considering the more diverse pyrolysis products, the higher degradation rate, and the less residues, the pyrolysis

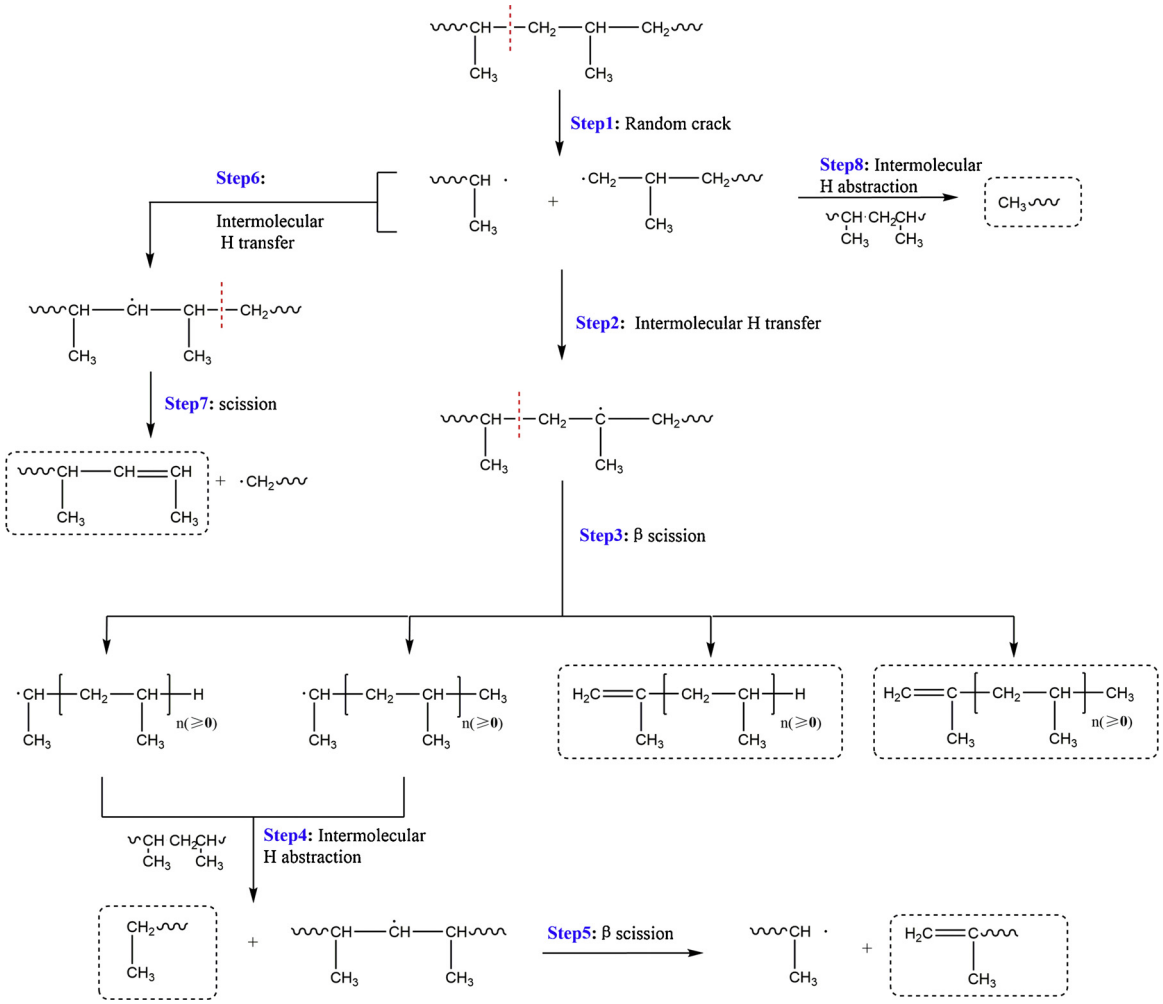

Fig. 9. The possible mechanism of the SY pyrolysis.

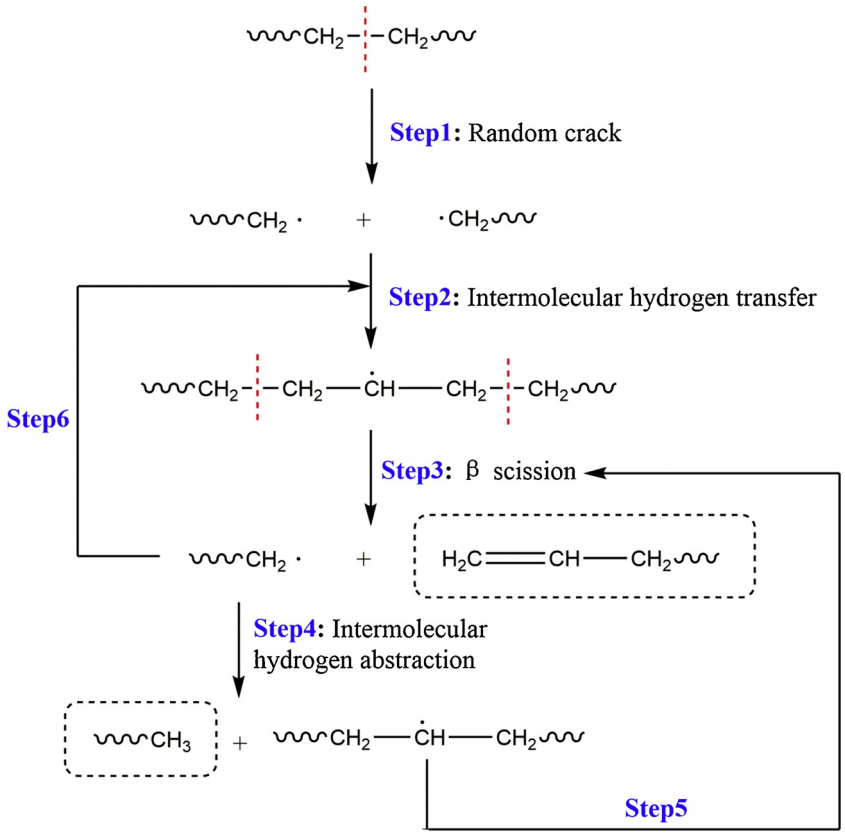

Fig. 10. The possible mechanism of the MB pyrolysis.

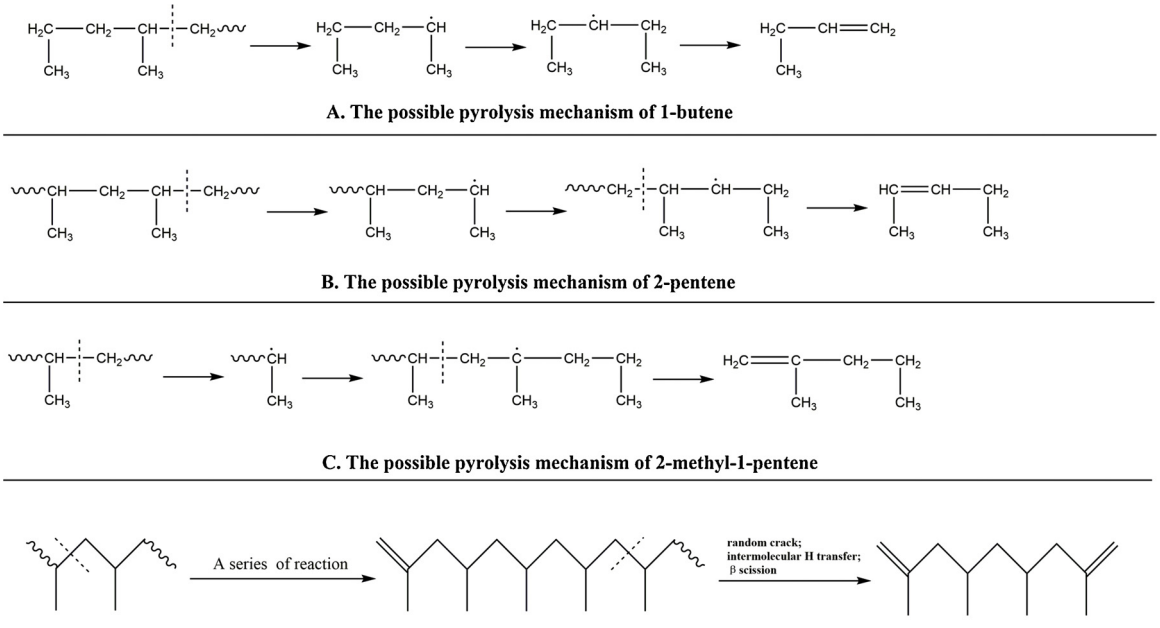

Fig. 11. The possible mechanisms of several SY pyrolysis products.

performance of MB appeared to be better than that of SY. However, the high proportion of alkenes and high-carbon-number long chains are a major obstacle for SY and MB to meet the fuel standard. Thus, the product selectivity of the SY, MB, or medical plastic waste pyrolysis needs to be improved through changing the reaction temperature and time and adding a catalyst, or co-pyrolysis in order to prepare fuel oils, or value-added chemical products (Anuar Sharuddin et al., 2016).

4. Conclusion

The pyrolytic behaviors, reaction mechanisms, pathways, and evolved gases of SY and MB were characterized in this study. The SY pyrolysis involved the devolatilization reaction in the range of 394.4 – 501 °C, while the MB pyrolysis mainly occurred at 417.9 – 517 °C. The most suitable reaction mechanism was determined as the

geometrical contraction model for the two SY pyrolysis stages and as the nucleation growth model for the MB pyrolysis. Even though the MB pyrolysis required more energy than did the SY pyrolysis, MB exhibited a better pyrolysis performance given their comprehensive analysis. The main pyrolytic volatiles were alkenes and a few long-chain alkanes and dienes for SY and alkenes and alkanes for MB. The possible pyrolysis pathways detected for SY and MB can provide the future research directions in terms of the thermochemical conversions of the medical (plastic) wastes. Overall, our findings can yield insights into the drivers, mechanisms, emissions, and energy and by-product recoveries as well as into waste stream reduction, pollution control, and reactor optimization associated with the pyrolysis of the medical plastic wastes.

CRediT authorship contribution statement

Ziyi Ding: Software, Investigation, Formal analysis, Writing - original draft, Writing - review & editing. **Huashan Chen:** Methodology, Formal analysis, Supervision, Validation. **Jingyong Liu:** Conceptualization, Methodology, Resources, Writing - review & editing, Project administration, Funding acquisition. **Haiming Cai:** Formal analysis, Investigation, Writing - review & editing. **Fatih Evrendilek:** Conceptualization, Software, Writing - review & editing. **Musa Buyukada:** Writing - review & editing.

Declaration of Competing Interest

The authors declare that they have no known competing financial interests or personal relationships that could have appeared to influence the work reported in this paper.

Acknowledgements

This work was financially supported by the National Natural Science Foundation of China (No. 51978175), and the Science and Technology Planning Project of Guangdong Province, China (No. 2016A040403071; 2017A040403059).

Appendix A. Supplementary data

Supplementary material related to this article can be found, in the online version, at doi:https://doi.org/10.1016/j.jhazmat.2020.123472.

References

Aboulkas, A., El harfi, K., El Bouadili, A., 2010. Thermal degradation behaviors of polyethylene and polypropylene. Part I: pyrolysis kinetics and mechanisms. Energ. Convers. Manage. 51, 1363–1369.
Ahmad, M.S., Mehmood, M.A., Liu, C.G., Tawab, A., Bai, F.W., Sakdaronnarong, C., Xu, J., Rahimuddin, S.A., Gull, M., 2018. Bioenergy potential of Wolffia arrhiza appraised through pyrolysis, kinetics, thermodynamics parameters and TG-FTIR-MS study of the evolved gases. Bioresour. Technol. Rep. 253, 297–303.
Anuar Sharuddin, S.D., Abnisa, F., Wan Daud, W.M.A., Aroua, M.K., 2016. A review on pyrolysis of plastic wastes. Energ. Convers. Manage. 115, 308–326.
Bujak, J.W., 2015. Heat recovery from thermal treatment of medical waste. Energy 90, 1721–1732.
Cai, H., Liu, J., Xie, W., Kuo, J., Buyukada, M., Evrendilek, F., 2019. Pyrolytic kinetics, reaction mechanisms and products of waste tea via TG-FTIR and Py-GC/MS. Energ. Convers. Manage. 184, 436–447.
Chen, T., Li, X., Yan, J., Jin, Y., 2009. Polychlorinated biphenyls emission from a medical waste incinerator in China. J. Hazard. Mater. 172, 1339–1343.
Chen, Y., Zhao, R., Xue, J., Li, J., 2013. Generation and distribution of PAHs in the process of medical waste incineration. Waste Manage. 33, 1165–1173.
Chen, J., Mu, L., Jiang, B., Yin, H., Song, X., Li, A., 2015. TG/DSC-FTIR and Py-GC investigation on pyrolysis characteristics of petrochemical wastewater sludge. Bioresour. Technol. Rep. 192, 1–10.
Chen, X., Liu, L., Zhang, L., Zhao, Y., Qiu, P., 2019. Gasification reactivity of co-pyrolysis char from coal blended with corn stalks. Bioresour. Technol. Rep. 279, 243–251.
Chen, J., Zhang, J., Liu, J., He, Y., Evrendilek, F., Buyukada, M., Xie, W., Sun, S., 2020. Co-pyrolytic mechanisms, kinetics, emissions and products of biomass and sewage sludge in N2, CO2 and mixed atmospheres. Chem. Eng. J. 397, 125372.
Deng, N., Zhang, Y., Wang, Y., 2008. Thermogravimetric analysis and kinetic study on pyrolysis of representative medical waste composition. Waste Manage. 28, 1572–1580.
Duan, H., Huang, Q., Wang, Q., Zhou, B., Li, J., 2008. Hazardous waste generation and management in China: a review. J. Hazard. Mater. 158, 221–227.
Fang, S., Yu, Z., Lin, Y., Hu, S., Liao, Y., Ma, X., 2015. Thermogravimetric analysis of the co-pyrolysis of paper sludge and municipal solid waste. Energ. Convers. Manage. 101, 626–631.
Fang, S., Jiang, L., Li, P., Bai, J., Chang, C., 2020. Study on pyrolysis products characteristics of medical waste and fractional condensation of the pyrolysis oil. Energy 195, 116969.
Hong, J., Zhan, S., Yu, Z., Hong, J., Qi, C., 2018. Life-cycle environmental and economic assessment of medical waste treatment. J. Clean. Prod. 174, 65–73.
Hu, J., Yan, Y., Evrendilek, F., Buyukada, M., Liu, J., 2019. Combustion behaviors of three bamboo residues: gas emission, kinetic, reaction mechanism and optimization patterns. J. Clean. Prod. 235, 549–561.
Irmak Aslan, D., Parthasarathy, P., Goldfarb, J.L., Ceylan, S., 2017. Pyrolysis reaction models of waste tires: application of master-plots method for energy conversion via devolatilization. Waste Manage. 68, 405–411.
Kai, X., Li, R., Yang, T., Shen, S., Ji, Q., Zhang, T., 2017. Study on the co-pyrolysis of rice straw and high density polyethylene blends using TG-FTIR-MS. Energ. Convers. Manage. 146, 20–33.
Lee, T., Oh, J., Kim, T., Tsang, D., Kim, K., Lee, J., Kwon, E., 2018. Controlling generation of benzenes and polycyclic aromatic hydrocarbons in thermolysis of polyvinyl chloride in CO_2. Energ. Convers. Manage. 164, 453–459.
Lijuan, Z., Fu-Shen, Z., Mengjun, C., Zhengang, L., Jianzhi, W.D.B., 2010. Typical pollutants in bottom ashes from a typical medical waste incinerator. J. Hazard. Mater. 173, 181–185.
Lin, Y., Liao, Y., Yu, Z., Fang, S., Ma, X., 2017. A study on co-pyrolysis of bagasse and sewage sludge using TG-FTIR and Py-GC/MS. Energ. Convers. Manage. 151, 190–198.
Luda, M.P., Dall'Anese, R., 2014. On the microstructure of polypropylenes by pyrolysis GC–MS. Polym. Degrad. Stabil. 110, 35–43.
Ma, C., Sun, L., Jin, L., Zhou, C., Xiang, J., Hu, S., Su, S., 2015. Effect of polypropylene on the pyrolysis of flame retarded high impact polystyrene. Fuel Process. Technol. 135, 150–156.
Ma, W., Rajput, G., Pan, M., Lin, F., Zhong, L., Chen, G., 2019. Pyrolysis of typical MSW components by Py-GC/MS and TG-FTIR. Fuel 251, 693–708.
Maia, A.A.D., de Morais, L.C., 2016. Kinetic parameters of red pepper waste as biomass to solid biofuel. Bioresour. Technol. Rep. 204, 157–163.
MEPC, 2019. Annual Report on Prevention and Control of Environmental Pollution by Solid Waste in Large, Medium and Large Cities in 2019. Ministry of environmental protection of the People's Republic of China.
Minh Loy, A.C., Yusup, S., Fui Chin, B.L., Wai Gan, D.K., Shahbaz, M., Acda, M.N., Unrean, P., Rianawati, E., 2018. Comparative study of in-situ catalytic pyrolysis of rice husk for syngas production: kinetics modelling and product gas analysis. J. Clean. Prod. 197, 1231–1243.
Moya, E.L., Thelakkadan, A.S., Sesto, E.V., Gómez-Elvira, J.M., 2011. The role of microstructure in the pyrolysis of polypropylene. A preliminary study on the syndiotactic stereoisomer. Polym. Degrad. Stabil. 96, 1087–1096.
Muneer, B., Zeeshan, M., Qaisar, S., Razzaq, M., Iftikhar, H., 2019. Influence of in-situ and ex-situ HZSM-5 catalyst on co-pyrolysis of corn stalk and polystyrene with a focus on liquid yield and quality. J. Clean. Prod. 237, 117762.
Qiao, Y., Wang, B., Zong, P., Tian, Y., Xu, F., Li, D., Li, F., Tian, Y., 2019. Thermal behavior, kinetics and fast pyrolysis characteristics of palm oil: analytical TG-FTIR and Py-GC/MS study. Energ. Convers. Manage. 199, 111964.
Qin, L., Han, J., Zhao, B., Wang, Y., Chen, W., Xing, F., 2018. Thermal degradation of medical plastic waste by in-situ FTIR, TG-MS and TG-GC/MS coupled analyses. J. Anal. Appl. Pyrol. 136, 132–145.
Sharuddin, S.D.A., Abnisa, F., Daud, W.M.A.W., Aroua, M.K., 2016. A review on pyrolysis of plastic wastes. Energ. Convers. Manage. 115, 308–326.
Singh, B., Sharma, N., 2008. Mechanistic implications of plastic degradation. Polym. Degrad. Stabil. 93, 561–584.
Singh, R.K., Ruj, B., Sadhukhan, A.K., Gupta, P., 2019. A TG-FTIR investigation on the co-pyrolysis of the waste HDPE, PP, PS and PET under high heating conditions. J. Energy Inst. 1020–1035.
Song, Y., Hu, J., Liu, J., Evrendilek, F., Buyukada, M., 2020. CO2-assisted co-pyrolysis of textile dyeing sludge and hyperaccumulator biomass: dynamic and comparative analyses of evolved gases, bio-oils, biochars, and reaction mechanisms. J. Hazard. Mater. 400, 123190.
Straka, P., Bičáková, O., Šupová, M., 2017. Thermal conversion of polyolefins/polystyrene ternary mixtures: kinetics and pyrolysis on a laboratory and commercial scales. J. Anal. Appl. Pyrol. 128, 196–207.
Sun, G., Zhang, G., Liu, J., Xie, W., Evrendilek, F., Buyukada, M., 2019. (Co-)combustion behaviors and products of spent potlining and textile dyeing sludge. J. Clean. Prod. 224, 384–395.
Wang, J., Shen, J., Ye, D., Yan, X., Zhang, Y., Yang, W., Li, X., Wang, J., Zhang, L., Pan, L., 2020. Disinfection technology of hospital wastes and wastewater: suggestions for disinfection strategy during coronavirus Disease 2019 (COVID-19) pandemic in China. Environ. Pollut. 262, 114665.
Windfeld, E.S., Brooks, M.S., 2015. Medical waste management - a review. J. Environ. Manage. 163, 98–108.
Wu, J., Chen, T., Luo, X., Han, D., Wang, Z., Wu, J., 2014. TG/FTIR analysis on co-pyrolysis behavior of PE, PVC and PS. Waste Manage. 34, 676–682.
Xu, F., Wang, B., Yang, D., Ming, X., Jiang, Y., Hao, J., Qiao, Y., Tian, Y., 2018a. TG-FTIR and Py-GC/MS study on pyrolysis mechanism and products distribution of waste bicycle tire. Energ. Convers. Manage. 175, 288–297.
Xu, F., Wang, B., Yang, D., Hao, J., Qiao, Y., Tian, Y., 2018b. Thermal degradation of

typical plastics under high heating rate conditions by TG-FTIR: pyrolysis behaviors and kinetic analysis. Energ. Convers. Manage. 171, 1106–1115.
Yan, J.H., Zhu, H.M., Jiang, X.G., Chi, Y., Cen, K.F., 2009. Analysis of volatile species kinetics during typical medical waste materials pyrolysis using a distributed activation energy model. J. Hazard. Mater. 162, 646–651.
Yang, Y., Peng, F., Wang, R., Guan, K., Jiang, T., Xu, G., Sun, J., Chang, C., 2020. The deadly coronaviruses: the 2003 SARS pandemic and the 2020 novel coronavirus epidemic in China. J. Autoimmun. 109, 102434.
Zhang, J., Liu, J., Evrendilek, F., Zhang, X., Buyukada, M., 2019. TG-FTIR and Py-GC/MS analyses of pyrolysis behaviors and products of cattle manure in CO_2 and N_2 atmospheres: kinetic, thermodynamic, and machine-learning models. Energ. Convers. Manage. 195, 346–359.
Zhang, L., Gong, Q., Duan, F., Chyang, C., Huang, C., 2020. Emissions of gaseous pollutants, polychlorinated dibenzo-p-dioxins, and polychlorinated dibenzo-furans from medical waste combustion in a batch fluidized-bed incinerator. J. Energy Inst. 93, 1428–1438.
Zhou, X., Broadbelt, L.J., Vinu, R., 2016. Chapter Two - mechanistic understanding of thermochemical conversion of polymers and lignocellulosic biomass. In: In: Van Geem, K.M. (Ed.), Advances in Chemical Engineering 49. Academic Press, pp. 95–198.
Zhu, H.M., Yan, J.H., Jiang, X.G., Lai, Y.E., Cen, K.F., 2008. Study on pyrolysis of typical medical waste materials by using TG-FTIR analysis. J. Hazard. Mater. 153, 670–676.
Zou, H., Evrendilek, F., Liu, J., Buyukada, M., 2019. Combustion behaviors of pileus and stipe parts of Lentinus edodes using thermogravimetric-mass spectrometry and Fourier transform infrared spectroscopy analyses: thermal conversion, kinetic, thermodynamic, gas emission and optimization analyses. Bioresour. Technol. Rep. 288, 121481.